Journal of Materials Chemistry A

Nano-fibrillated Cellulose/Al(OH)3/Polytetrafluoroethylene Hybrid Protective Layer Enabling Dendrite Free Zn Anodes for Rechargeable Aqueous Batteries

Journal:	*Journal of Materials Chemistry A*
Manuscript ID	TA-ART-09-2023-005655.R1
Article Type:	Paper
Date Submitted by the Author:	26-Nov-2023
Complete List of Authors:	Shayan, Mohammad; Louisiana State University Abouzeid, Ragab; Louisiana State University Xu, Wangwang; Louisiana State University System Wu, Tongyao ; Louisiana State University Wu, Qinglin; Louisiana State University, RNR

Nanofibrillated Cellulose/$Al(OH)_3$/Polytetrafluoroethylene Hybrid Protective Layer Enabling Dendrite Free Zn Anodes for Rechargeable Aqueous Batteries

Mohammad Shayan[1], Ragab Abouzeid[1,2], Wangwang Xu[1*], Tongyao Wu[3] and Qinglin Wu[1*]

[1] School of Renewable Natural Resources, Louisiana State University AgCenter, Baton Rouge, LA 70803, United States

[2] Cellulose and Paper Department, National Research Centre, 33 Bohouth St., Dokki, Giza 12622, Egypt

[3] Department of Electrical and Computer Engineering, Louisiana State University, Baton Rouge, LA 70803, United States

Corresponding E-mail: wuqing@lsu.edu and wxu26@lsu.edu

Abstract

Aqueous zinc ion batteries (ZIBs) are considered as promising options for energy storage devices due to their high safety and abundant resources. However, Zn dendrites and short-circuit pose a significant challenge. To address this issues, a hybrid protective membrane of nanofibrillated cellulose (NFC)/$Al(OH)_3$/ Polytetrafluoroethylene (PTFE) was fabricated and coated on the surface of zinc metal anode. The in-situ formation of $Al(OH)_3$ nanoparticles created nano pores inside the dense NFC network, while the addition of PTFE improved the adhesion of protective membrane to the surface of zinc metal. The NFC/$Al(OH)_3$/PTFE coating layer restricted the active water and anions from the electrode/electrolyte interface by dehydrating zinc ions, thus preventing water and anion-induced corrosions. With the NFC/$Al(OH)_3$/PTFE coating layer, zinc symmetric batteries exhibited significantly improved cycling performance with highly stabilized charge/discharge profiles, outperforming bare zinc symmetric batteries. Furthermore, full vanadium dioxide (VO_2)||NFC/ $Al(OH)_3$/PTFE @Zn batteries demonstrated a high initial specific capacity of 406.2 mAh g^{-1} at 2 A g^{-1} and excellent

cycling stability with a 94% retention of intial capacity after 300 cycles , and 72% after 3300 cycles, making them practical for energy storage applications.

***Keywords**:* Zn ion battery, dendrite-free anode, inhibit water-induced corrosion, protective coating layer

1. Introduction

Fast depletion of unsustainable fossil fuels (i.e., coal, oil, and gas) and their detrimental impacts on the environment along with growing population have increased the demand for alternative green energies such as solar, wind, geothermal, and biofuels[1,2]. With the wide utilization of intermittently available solar and wind energy, there is an urgent need for the development of grid-scale energy storage devices that are safe, reliable, and low-cost [3,4]. Despite the excellent performance of lithium-ion batteries in some applications, their application is limited in grid-scale energy storage systems due to their safety issues and high cost [5]. Hence, rechargeable aqueous zinc-ion batteries (ZIBs) have attracted increasing attention widely owing to safety, low toxicity, and abundant raw materials [4,6]. Due to its low cost and the ability for industrial manufacturing, Zn metal is widely employed as the anode for ZIBs. Moreover, its high volumetric capacity (5854 mAh/cm^3), high gravimetric capacity (820 mAh/g), and low redox potential (-0.76 V *vs* standard hydrogen electrode) has made the Zn metal an appropriate anode for next-generation energy storage technologies [4,7]. However, one of the main challenges in developing commercial Zn metal anodes is the formation of dendrites. When Zn^{2+} ions are deposited onto the surface of the anode during the plating process, they frequently build up protrusions due to their high surface energy. This leads to the formation and continued growth of Zn dendrites, which can penetrate through the separator, causing a short-circuit failure [8,9]. The application of ZIBs is also hindered by the unstable Zn anode/electrolyte interface due to the

water-induced hydrogen evolution reaction (HER) and chemical corrosions, decreasing the Coulombic efficiency and cycling lifetime of ZIBs [7,10].

In order to address the abovementioned problems, some strategies have been employed, including using Zn alloys [11], constructing artificial interfaces [10,12,13], modifying electrolytes using electrolyte additives [14,15,16], and fabricating functional separators [17,18]. Among them, the addition of a protective interface layer as an artificial interface is a promising approach to make the surface electric field uniform and prevent the dendrite formation on the Zn anode. An artificial coating layer with appropriate stability in aqueous electrolyte, good ionic conductivity, and uniform porosity can regulate the deposition of Zn ions on the Zn anode surface [15,19,20].

As natural organic polymers, cellulose nanomaterials (CNMs) are produced after the chemical and physical treatment of sustainable fiber sources from trees, plants, sugarcane, and other biomass. CNMs have two main forms – nanofibrillated cellulose (NFC) and cellulose nanocrystals (CNCs), which can be used for different applications [21,22]. Favorable properties of CNMs including high mechanical strength, hydrophilicity, and biodegradation rate have made CNMs an appropriate material for use in energy storage devices such as ZIBs [17,23,24]. With further development, CNMs can be used as coating suspensions and separators to inhibit dendrite growth on the zinc anode of ZIBs and improve their performance [17,25]. Moreover, utilizing cellulose-based materials as a sustainable protective layer prevents water-induced side reactions such as hydrogen evolution reactions in the electrode-electrolyte interface to further improve the cycling performance of ZIBs [20,26,27]. Liu et al. [10] used lignin-containing cellulose nanofiber (LCNF) and MXene (LM) to enhance the stability of the zinc anode interface. Their results revealed that LCNF component offers considerable mechanical strength, preventing the dendrite growth due to limited diffusion. Meanwhile, MXene plays a role as a zinc gating layer,

facilitating the movement of zinc ions, guiding the deposition of zinc ions along the (002) plane. Guo et al.[30] developed a porous zinc electrode coated with polytetrafluoroethylene (PTFE) for improved performance in zinc-ion batteries. Their result showed that the addition of PTFE has several positive effects: it suppressed the hydrogen evolution reaction, ensuring the stability of the zinc metal anode; it enabled dendrite-free zinc platin, enhancing long-term battery performance; and it contributed to improved cycling performances of the Zn||V_2O_5 battery, thanks to the artificial layer provided by the PTFE coating. Therefore, in order to investigate the zinc anode dendrite suppression, active water restriction, and corrosion prevention, an ideal protective layer would need to combine a sustainable porous material with an artificial protective layer to suppress dendrite formation and ameliorate the cycling performance of Zn-ion battery.

Herein, the main objective of this study is to develop a novel nanofibrillated cellulose (NFC)/$Al(OH)_3$/PTFE protective layer to hinder the growth of dendrites, regulate the deposition of Zn^{2+} ions, and stabilize the Zn metal anode in ZIBs. The hydrophilic NFC layer absorbs the free water molecules and prevents water-induced corrosion reactions in electrode-electrolyte interface. In addition, the in-situ formation of $Al(OH)_3$ nanoparticles increases the porosity of NFC network interfacial layer and improves the electrolyte uptake. Moreover, $Al(OH)_3$ nanoparticles can effectively fill the spaces between cellulose nanofibers, resulting to a higher surface area and increased formation of voids within the film structure, thereby enhancing porosity. The porous structure of NFC network, as uniform channels, has a shunt effect on Zn ions, which provides position selected uniform ion transportation and even electrochemical deposition. The addition of PTFE to the coating suspension ameliorates the adhesion of NFC/$Al(OH)_3$ suspension to the surface of Zn metal. Finally, the aforementioned mechanisms prevent the dendrite growth of zinc, enhance the cycling life and stability of ZIBs.

94 **2. Experimental section**

95 **2.1. Materials**

96 Commercially grade NFC (15 wt.% solid concentration) was purchased from the
97 University of Maine (Orono, ME, USA). Ethanol (98%) and oxalic acid dihydrate (>99%) were
98 purchased from Fisher Scientific Co (Hampton, NH, USA). Carbon black powder (CB 60),
99 Polytetrafluoroethylene (PTFE) (Condensed Liquid Binder, EQ-Lib-PTFE), and coin-type cell
100 parts (CR2032) were supplied by MTI corporation (Richmond, CA, USA).

101 **2.2. Preparation of NFC/Al $(OH)_3$/PTFE coating suspension**

102 NFC material (3.5 g) was first added to 100 ml NaOH solution (2 wt.%) and the
103 suspension was stirred for one hour. In situ synthesis of Al $(OH)_3$ was performed by the addition
104 of 0.05 g Al foil to the as-prepared alkaline NFC suspension and the mixture was stirred for 24 h
105 at room temperature. Then, hydrochloric acid (HCl) was added to the mixture to decrease pH,
106 accelerate the hydrolysis reaction, and facilitate the conversion of sodium aluminate into
107 aluminum hydroxide. After that, the suspension was rinsed with deionized (DI) water and
108 centrifuged three times at 10000 rpm for 7 minutes. Finally, the as-obtained cake material was
109 dispersed in DI water to form the NFC/Al $(OH)_3$ suspension. The coating suspension was
110 prepared by the addition of PTFE (1:1 weight ratio based on the dried NFC) followed by stirring
111 and sonication for 1 h. Finally, the suspension was casted onto the surface of circle bare zinc
112 foils (diameter = 0.8 cm) and dried at room temperature (25 ˚C) for 24 h. The mass ratio between
113 the protective layer and the zinc anode foil was around 0.028 and the thickness of the protective
114 layer was around 20 μm.

115 **2.3. Preparation of VO_2 nanofibers**

The VO_2 nanofibers were prepared based on the method by Xu et al. [19]. First, oxalic acid (5 g) was dissolved and stirred in 60 mL deionized water. Then, 2.5 g divanadium pentoxide (V_2O_5) was added into the solution. The solution was stirred at 25 °C for 1 h to obtain a transparent blue solution. The solution was then transferred to a Teflon-lined autoclave for heating at 180 °C for 12 h. Then, the precipitated material was collected with centrifugation and washed with deionized water and ethanol for three times respectively. The final product was obtained after drying at 70 °C for 24h.

2.4. Material characterization

The XRD analysis was conducted using a PANalytical Empyrean X-ray Diffractometer (Malvern Panalytical Ltd., Malvern, Worcestershire, UK) equipped with a CuKα radiation source (λ = 0.15418 nm) at 45 kV and 40 mA with the 2θ range from 5° to 90° and a scan rate of 1° per minute to evaluate the crystal structure of hybrid coating material. The surface and cross-section morphologies of coated Zn foils were observed by Quanta™ 3D DualBeam™ FEG FIB-SEM (FEI Co, Eindhoven, Netherlands) at an acceleration voltage of 20 kV. Prior to SEM observations, a sputter-coater was used to coat the samples with Pt. The morphology of $Al(OH)_3$ nanoparticles and NFC was analyzed using transmission electron microscope (TEM) (JEM 1400, JEOL Inc., Peabody, MA, USA) with an accelerating voltage of 120 kV. Prior to TEM imaging, each suspension was diluted to 0.002 wt. % using deionized water and subjected to a 30-minute ultrasonic treatment. The Atomic Force Microscopy (AFM) observations were conducted using a Bruker Dimension Icon XR (Bruker Nano Inc, Tucson, AZ, USA). The energy-dispersive X-ray spectroscopy (EDS) was conducted to analyze the elemental compositions of the coating layer. Electrochemical impedance spectroscopy (EIS) data were gathered by applying an AC potential with an amplitude of 5 mV across a frequency range of 0.01-100 kHz. The measurement of the

porosity of the membranes was conducted using the following procedure. First, 3 circular specimens of NFC, as control, and NFC/$Al(OH)_3$/PTFE membrane were dried in an oven set at a temperature of 60°C for 24 hours and the weight of the dried samples (W_{dry}) and their thickness was measured. After that, specimens were completely submerged in ethanol for a duration of 5 hour. The specimens were removed from ethanol and wiped with a damp linen cloth saturated with ethanol. They were then promptly weighed in the to obtain the wet weight (W_{wet}). The porosity (P) of the membranes was subsequently determined by employing the following equation:

$$P\ (\%) = \frac{(W_{wet} - W_{dry})/\rho_e}{(W_{wet} - W_{dry})/\rho_e + W_{dry}/\rho_m} \quad (1)$$

where, W_{wet} and W_{dry} are the mass of the wet and the dry membranes, respectively, while ρ_e and ρ_m are the density of ethanol and the membrane, respectively.

2.5. Coin cell assembling and electrochemical measurement

For making full cell coin batteries, cathode was prepared by mixing a composition of as-prepared VO_2 nanofibers, carbon black, and PTFE binder with a weight ratio of (6:3:1) in ethanol, followed by grinding in a mortar and pestle. Glass fiber and 3M Zn $(CF_3SO_3)_2$ aqueous solution were used as the separator and electrolyte, respectively. The symmetric coin cell batteries were assembled using same bare and coated zinc foils as both anode and cathode to evaluate the stripping/plating behavior and cycling stability of the batteries. The galvanostatic charge-discharge (GCD) electrochemical tests were carried out on a multichannel LAND battery analyzer (CT3001A, LAND Electronics Corporation, Wuhan, China) with the voltage range of 0.2 - 1.6 V at room temperature. Cyclic voltammetry (CV) test was conducted on an electrochemical workstation (CHI 760e) in a potential range of 0.2-1.7 V.

3. Results and Discussion

Fig.1 shows the schematic of the in-situ formation process of $Al(OH)_3$ nanoparticles in the NFC and the coating process of hybrid NFC/Al $(OH)_3$/PTFE as a protective interface layer on the bare zinc foil. The spacing between the cellulose molecular chains and the hydrogen bonding between $Al(OH)_3$ and NFC can facilitate the transfer of Zn^{2+} ions through the interface layer.

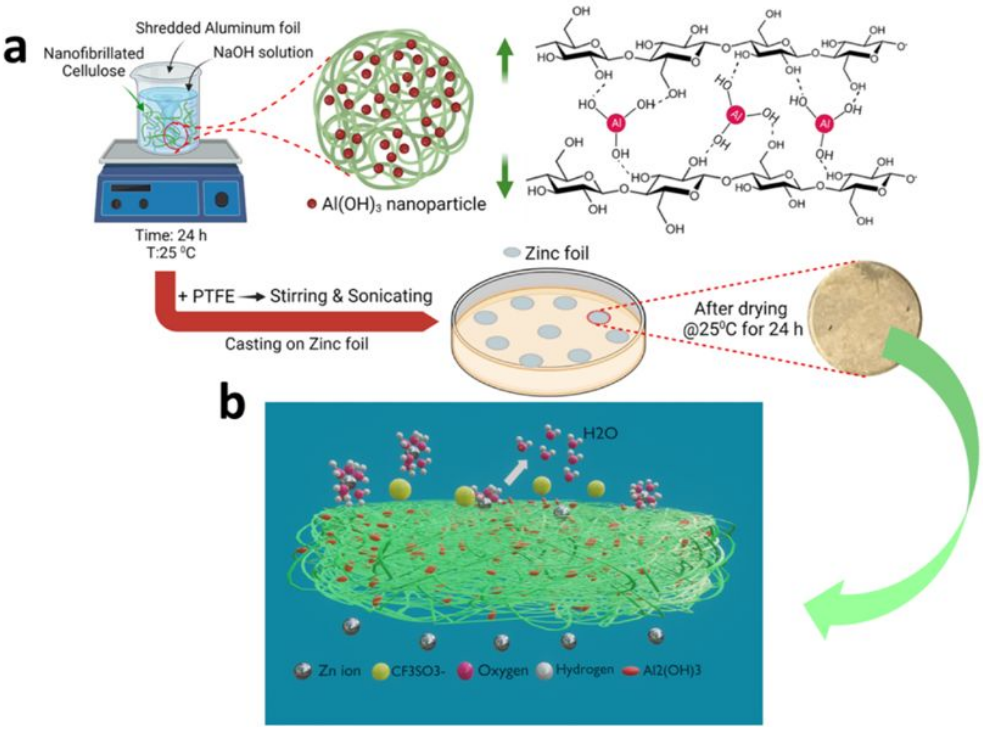

Fig.1. Schematic illustration of (a) in-situ fabrication of $Al(OH)_3$ nanoparticles in NFC, and coating Zn foil using the NFC/$Al(OH)_3$/PTFE suspension as a hybrid protective layer, and (b) the membrane's ion sieving mechanism illustrating how the movement of the bulky hydrated $CF_3SO_3^-$ anion and water molecules within the hydrated Zn^{2+} being impeded.

The cross-section and surface morphology of the NFC/$Al(OH)_3$/PTFE coated Zn is displayed in Fig.2 (a-d). The detached coated membrane from the Zn surface after cutting shows

the PTFE fibers, which confirms the appropriate adhesion of hybrid membrane on the surface of Zn anode. The $Al(OH)_3$ nanoparticles and micro/nano porous structure of coated membrane are shown in Fig. 2 (b-d). The in-situ synthesis of $Al(OH)_3$ nanoparticles renders the establishment of interconnected nanoscale tortuous channels inside the dense NFC. Transmission Electron Microscopy (TEM) was employed to observe the distribution of nanoparticles within the NFC matrix, as is shown in Fig. S1 (supporting information). TEM images illustrate the well-distributed nanoparticles within the NFC matrix, showcasing a uniform dispersion throughout the naofibrillated cellulose. AFM was use to provide more details of protective layer 's topographical features as is shown in Fig. S2. Low heights (dark colors) in Fig. S2a represent regions of the surface of protective layer that are lower in height, indicating smoother or less textured surface. High heights (bright colors) represent elevated features on the sample surface such as NFC, Al(OH)3 nanoparticles, or other topographical variations during the casting of the protective layer. The color gradient in Fig S2b, corresponding to the force values ranging from -8.3 to 8 nN, represents the varying forces between the AFM tip and the sample surface during scanning. Bright areas indicate strong adhesion or interaction forces and dark areas suggest smoother, reduced adhesion or minimal interaction between the tip and the surface of protective layer. The results of porosity measurements revealed that the porosity of NFC/$Al(OH)_3$/PTFE membrane is around 53.1 ± 3.6% which is considerably higher than the porosity of neat NFC membrane (23.1± 6.7 %). EDS elemental mappings as shown in Fig 2. (e-g) confirm that the elements C, Al, O, and F are uniformly distributed in the coated hybrid membrane. The recorded EDS spectrum of coated material is shown in Fig. 2 h. The strong signal of Al element supports the in-situ synthesis of $Al(OH)_3$ nanoparticles inside the NFC suspension. The crystalline structure of NFC/$Al(OH)_3$/PTFE protective layer was evaluated by XRD, as shown in Fig. 2j. The results

197 revealed that both NFC and NFC/$Al(OH)_3$/PTFE membrane show cellulose Iβ crystalline
198 structure with different intensities, where the main characteristic peaks at 16.4˚ (110), 22.6˚
199 (200), and 34.5˚ (004) can be observed [21]. The sharp peak at around 2θ=18.1˚ could be attributed
200 to the crystalline structure of PTFE corresponding to diffraction in the (100) plane [28]. $Al(OH)_3$
201 nanoparticles also exhibit a dominant narrow peak around 18.1˚ corresponding to the (002)
202 crystal plane of monoclinic phase. Moreover, the small narrow peak at 2θ=28.6˚ can be ascribed
203 to the (202) plane of crystallized in-situ prepared $Al(OH)_3$ nanoparticles. The XRD pattern of
204 separately prepared pure $Al(OH)_3$ nanoparticles and PTFE is shown in Fig. S3. The pattern of the
205 $Al(OH)_3$ nanoparticles matches the literature values, demonstrating their high degree of
206 crystallinity [29]. The presence of narrow and sharp peaks further confirms the well-defined
207 crystalline structure of the $Al(OH)_3$ nanoparticles. Moreover, the synthesis of $Al(OH)_3$ was
208 confirmed by observing the formation of a distinct white precipitate resulting from the reaction.
209 The emergence of this white precipitate provided further evidence that $Al(OH)_3$ was successfully
210 synthesized in the process. The contact angle measurement was conducted using 3 M
211 $Zn(CF_3SO_3)_2$ electrolyte solution on the bare zinc foil and the NFC/$Al(OH)_3$/PTFE coated Zn
212 foil. As demonstrated in Fig. 2 (k,l), the contact angle of NFC/$Al(OH)_3$/PTFE @ Zn (29.7°) is
213 much lower in comparison with the contact angle of bare Zn foil (86.1°), reflecting its enhanced
214 wettability and electrolyte affinity due to the presence of abundant hydroxyl groups in the coated
215 hybrid layer. The cellulose, which possesses numerous surface functional groups such as C-OH
216 and C-COOH, is believed to undergo deprotonation in the electrolyte. This deprotonation process
217 enhances the cellulose's affinity for cations, thereby facilitating their adsorption and flux across
218 the membrane, while exhibiting the less tendency for anions. This mechanism can effectively
219 prevent the occurrence of the anion decomposition or corrosion reaction. In the $Zn(CF3SO3)_2$

electrolyte, each Zn^{2+} ion is bound to six H_2O molecules, which imparts an extremely high desolvation energy to Zn^{2+} [19]. When using NFC/$Al(OH)_3$/PTFE protective layer, Zn^{2+} initially coordinates with two C-OH terminals on the NFC backbone structure, followed by coordination with H_2O molecules, leading to the desolvation process. As illustrated in Fig. 1, the protective layer can capture active water molecules and prevent them from reaching the electrolyte/electrode interface, which can facilitate improved kinetics of Zn plating/stripping. This implies that a desolvation and ion-selective membrane are advantageous for enhancing the performance of zinc metal batteries [19].

The Zn plating/stripping electrochemical performance was studied using symmetric Zn||Zn batteries with and without NFC/$Al(OH)_3$/PTFE coating layers. Fig. 3a demonstrates the cycling performance of symmetric bare Zn and NFC/$Al(OH)_3$/PTFE @ Zn cells at 2.5 mA/cm^2, 0.5 mAh/cm^2. Symmetric NFC/$Al(OH)_3$/PTFE @Zn cell exhibits stable cycling and smooth voltage profile for over 260 h. However, using the bare Zn in the symmetric cell causes unstable charge/discharge cycling at the beginning and rapid short circuit after only 20 hours. The long cycling properties of symmetric bare Zn and NFC/$Al(OH)_3$/PTFE @ Zn cells at 1 mA/cm^2 are shown in Fig.3b. The results illustrate that NFC/$Al(OH)_3$/PTFE coating on the zinc surface

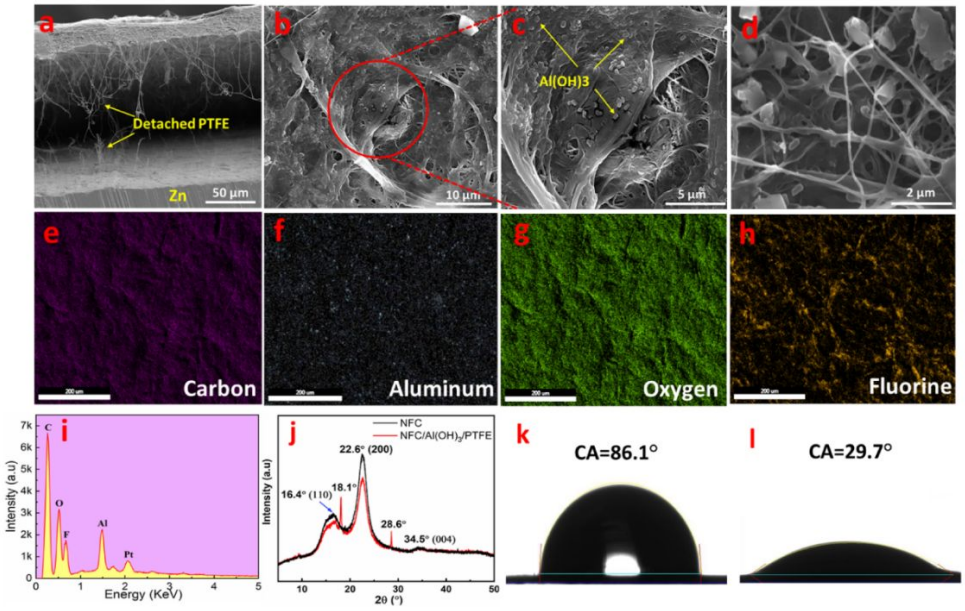

Fig. 2. Material characteristics of the NFC/$Al(OH)_3$/PTFE coating layer: (a) SEM images of cross-section of coated Zn with NFC/$Al(OH)_3$/PTFE, (b-d) surface of the NFC/$Al(OH)_3$/PTFE coating layer, EDS mapping (e-h), EDS spectrum of prepared NFC/$Al(OH)_3$/PTFE membrane (i), XRD patterns of pure NFC membrane and NFC/$Al(OH)_3$/PTFE coating layer (j), contact angles on bare zinc anode (k) and coated Zn with NFC/$Al(OH)_3$/PTFE (l).

significantly enhances the stability and cycling life of the battery for over 1000 hours. Nevertheless, the battery without coating suffered from the sever fluctuations in the first 100 hours and short circuit occurred after around 500 hours. This fluctuation during the charge/discharge and rapid short circuit failure could be attributed to the irregular deposition and fast longitudinal growth of dendrites that penetrate through the separator. In order to understand the effectiveness of $Al(OH)_3$ nanoparticles and PTFE on the cycling performance of batteries, Zn//Zn symmetric batteries with NFC @Zn and PTFE @Zn coating layers were tested at 2.5 mA/cm^2 (0.5 mAh/cm^2), which are demonstrated in Fig. S4. The PTFE coating was applied on the surface of zinc plates through casting of PTFE emulsion (70 μl PTFE in 10 ml DI water). The

results revealed that the symmetric PTFE @Zn cell leads to relatively unstable charge/discharge cycling, higher overpotential, and eventually results in a short circuit within a mere 120 hours. The presence of the inert and insulating PTFE coating may impact the kinetics of Zn plating and stripping, leading to a higher overpotential and instability because of increased charge-transfer resistance. However, the application of pure PTFE coating addresses the issues related to hydrogen evolution and Zn corrosion. This synthetic PTFE layer serves multiple purposes, including facilitating controlled Zn^{2+} migration, promoting uniform nucleation of Zn metal, acting as a barrier against water and oxygen ingress and finally improve the cycling life of batteries [30]. The cycling of NFC @Zn symmetric batteries showed relatively more stable charge/discharge behavior and slightly higher cycling life around 150 cycles. The improved cycling life and stability could be attributed to the restriction of the access of active water and anions to the electrode/electrolyte interface, which effectively inhibits corrosion induced by water and anions. However, hybrid NFC/$Al(OH)_3$/PTFE coating, shows a prolonged and smooth cycling lifespan (Fig. 3a), which could be attributed to the combined effect of uniform and slow deposition of Zn^{+2} ions and lower probability of side reactions such as hydrogen evolution reaction (HER). On the other hand, the abundance of hydroxyl groups on the surface of NFC can promote the even deposition of Zn^{2+} on the anode (Q. Li et al., 2022; Z. Li et al., 2023). $Al(OH)_3$ nanoparticles create nano channels inside the dense structure of NFC network and its dual function as water-gating and zinc-sieving improves the uniform penetration of Zn^{2+} ions into the coated layer, resulting in evenly deposition of Zn^{2+} ions on the anode surface and prevent the growth of Zn dendrites. Moreover, NFC/$Al(OH)_3$/PTFE coating may also act as a kind of gel polymer electrolyte which can decrease the fast transfer of Zn^{2+} ions and prevent the rapid growth of dendrites [31]. The hybrid coating layer, as a solid-electrolyte interface, prevents the

direct contact of H_2O molecules and Zn anode surface and inhibits hydrogen evolution reaction [30,32]. In spite of improved cycling life and stability of the battery with coated Zn anode, the potential of symmetric NFC/$Al(OH)_3$/PTFE @Zn is only slightly higher than the symmetric bare Zn cell. The increased polarization potential can be ascribed to the sluggish behavior of Zn^{2+} desolvation on the NFC/$Al(OH)_3$/PTFE hybrid membrane because of the interactions between $Zn[(H2O)_6]^{+2}$ complex, $Al(OH)_3$ nanoparticles and abundant hydroxyl groups of NFC. Consequently, the Zn^{2+} ions cannot easily reach to the surface of anode, electron tunneling is reduced, and it needs more energy to break the Zn^{2+} solvation sheath [33]. In order to determine the optimal thickness for the protective layer, impedance spectroscopy (EIS) was conducted to assess the transfer impedance of Zn^{+2} at thicknesses of 10, 20, and 30 μm (Fig. S5a). The results revealed an increase in thickness corresponded to higher resistance, indicative of reduced ionic conductivity. Subsequently, the cycling stability of symmetric batteries was tested with protective layers of varying thicknesses at a current density of 2.5 mA/cm2 (0.5 mAh/cm2). as is shown in Fig. S5b. While the protective layer with a thickness of 10 μm demonstrated favorable ionic conductivity, as indicated by the EIS results, its cycling stability proved inadequate. Additionally, it did not effectively inhibit dendrite formation, leading to a short circuit. Conversely, the thickest protective layer exhibited low ionic conductivity, resulting in increased internal resistance within the battery. This increased resistance contributes to higher overpotentials during charge/discharge, leading to unstable charge/discharge and reduced cycling life. Furthermore, the low ionic conductivity hampers the transport of ions between the electrodes, impacting the kinetics of electrochemical reactions. This sluggish ion transport can manifest in slower charge/discharge rates and an overall decrease in the performance of

296 batteries[33]. These results highlighted that the 20 μm thickness exhibited an extended cycling life
297 with acceptable ion transportation, representing the optimized thickness.

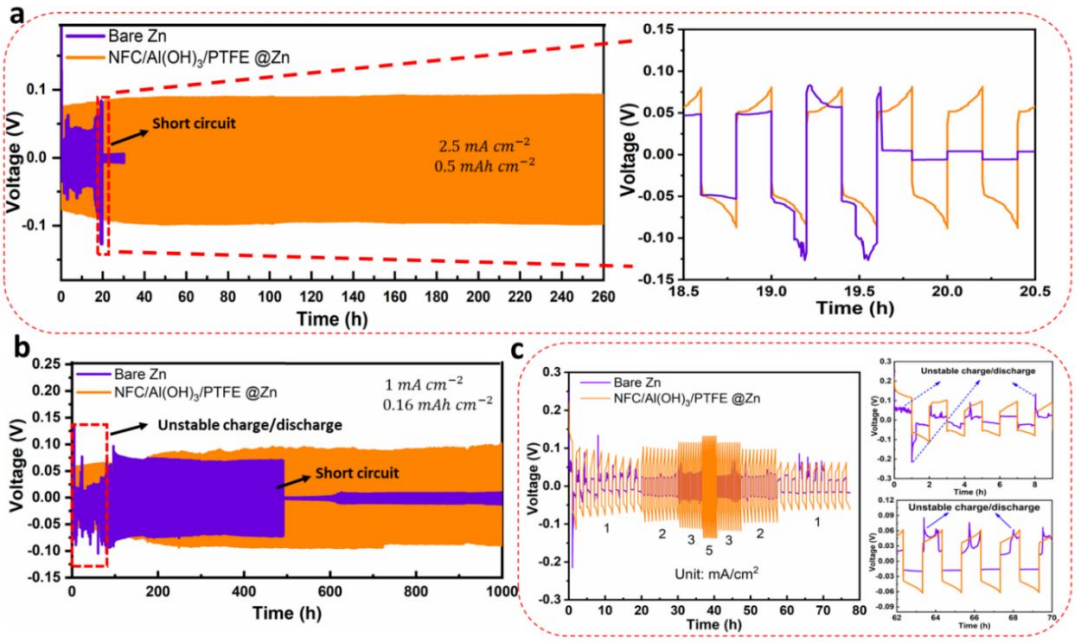

298

299 **Fig. 3.** Electrochemical behaviors of symmetric cells with bare Zn and NFC/Al(OH)$_3$/PTFE
300 @Zn: (a) cycling performance at different current densities of 2.5 mAcm^{-2}, (b) 1.0 mAcm^{-2}, and
301 (c) rate performance at various current densities of 1, 2, 3, 5, 3, 2, and 1 mAcm^{-2} at a fixed
302 capacity of 1 mAhcm^{-2}.

303 Fig. 3c shows the rate performance of the Zn symmetric batteries with and without
304 NFC/Al(OH)$_3$/PTFE coating layers at a fixed capacity of 1 mAh/cm^2. The results clearly show
305 that the batteries with NFC/Al(OH)$_3$/PTFE coated Zn anodes demonstrate a flat and stable
306 voltage plateau at each current density. While the coating of the Zn anode, as a solid-electrolyte
307 interface, regulates the deposition of Zn^{2+} ions and suppresses the parasitic side reaction, the
308 sluggish Zn^{2+} ions transfer can increase the polarization potential of batteries at all current
309 densities.

In order to investigate how the NFC/$Al(OH)_3$/PTFE coating layer affects the behavior of Zn plating, the morphology of Zn foils was examined with and without the coated layer after being plated for 1 hour at 1mA/cm^2. As illustrated in Fig. 4a-b, the bare zinc anode displayed significant spike shaped dendrites formation and distributed piles of Zn protrusions on its surface. The morphology of the Zn metal with the NFC/$Al(OH)_3$/PTFE coating layer, after partially removing the coated layer from the Zn anode, is displayed in Fig. 4c-d. The images demonstrate a flat and smooth deposition of Zn ions among NFC network and glass fibers, indicating that the deposition behavior of Zn on the NFC/$Al(OH)_3$/PTFE@Zn anode is distinct from that on its bare counterpart. Fig.4e provides a visual comparison of zinc deposition mechanisms, highlighting the differences between bare zinc and zinc coated with the NFC/$Al(OH)_3$/PTFE protective layer. It illustrates the distinct behaviors observed during zinc plating, emphasizing the impact of coating on deposition processes.

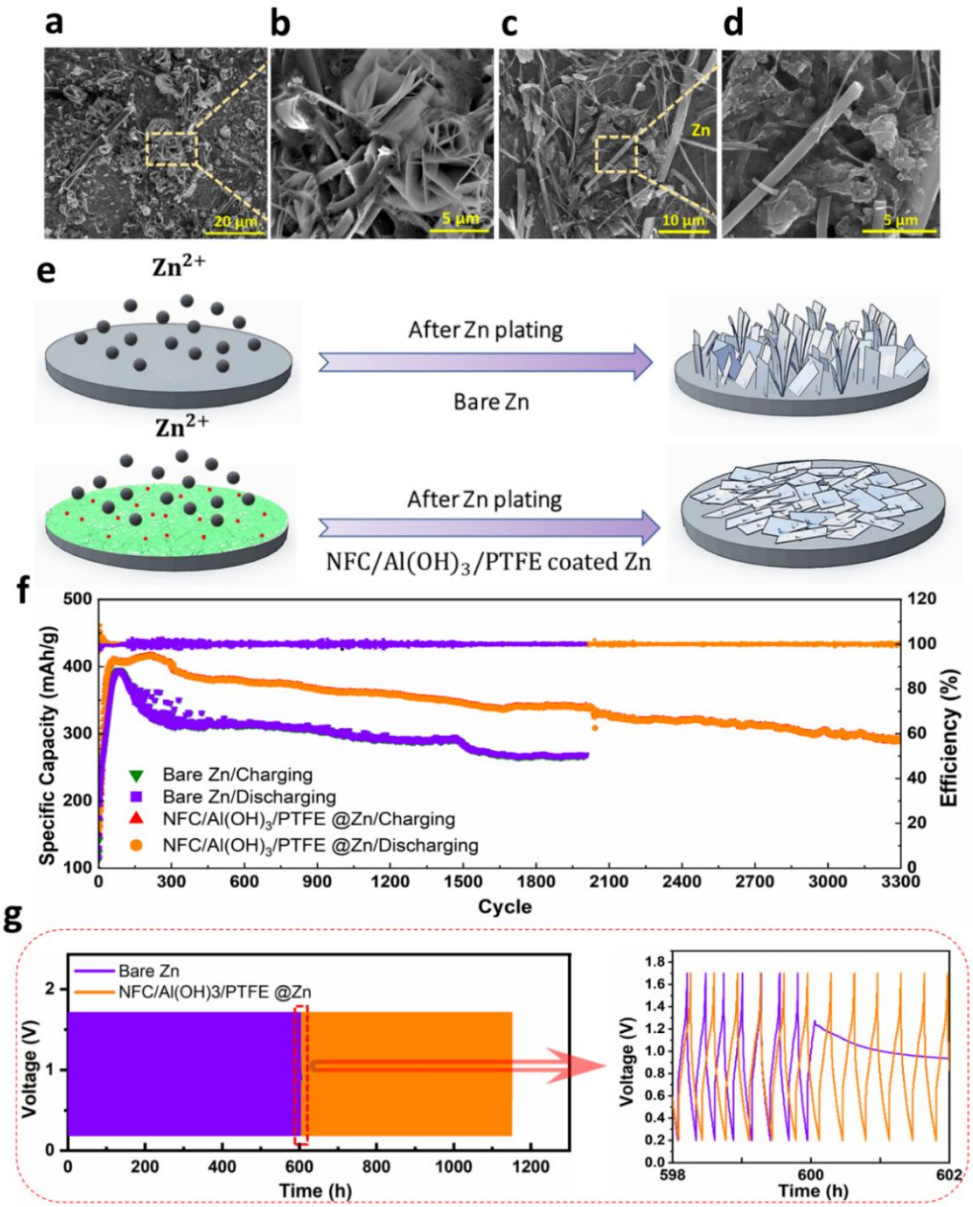

Fig. 4. Surface morphology of bare Zn anode (a, b) and NFC/Al(OH)$_3$/PTFE @Zn anode (c, d) after Zn plating for 1 hour at current density of 1 mA cm^{-2}. (e) Illustrative Schematics Unveiling the Zn Plating Behavior of bare Zn and coated Zn. Electrochemical behaviors of full cell batteries with bare Zn and NFC/Al(OH)$_3$/PTFE @Zn: (f) galvanostatic cycling performance at current density of 2.0 A/g, and (g) charge/discharge curves at current density of 2.0 A/g.

330 The Coulombic efficiencies (CEs) of Zn plating and stripping, which are crucial indicators of
331 redox reversibility, were examined using Zn//Cu coin cell configuration (Fig. S6). The voltage
332 profiles of the asymmetric cells at specific cycles at areal specific capacity of 1 mAh/cm^2 are
333 illustrated in Fig. S7. The Cu//NFC/Al(OH)$_3$/PTFE @Zn asymmetric batteries demonstrated
334 exceptional stability and consistently maintained an average Coulombic efficiency (CE) around
335 100.5% over an extended period of more than 400 cycles at a fixed plating capacity of 1
336 mAh/cm^2. In stark contrast, in the absence of protective layers, the CE value of the bare Zn//Cu
337 asymmetric cells deteriorates over approximately 180 cycles, demonstrating the intrinsic
338 instability in zinc striping and plating behaviors on the copper substrate. The substantial
339 enhancement in CE performance of can be ascribed to the presence of the NFC/Al(OH)$_3$/PTFE
340 hybrid protective layers, which effectively mitigate rapid formation of zinc dendrites, while
341 concurrently inhibiting detrimental side reactions.

342 The performance of NFC/Al(OH)$_3$/PTFE coated Zn was evaluated in practical
343 applications by assembling full cells using NFC/Al(OH)$_3$/PTFE @Zn as the anode and the
344 synthesized VO_2 nanofibers as the cathode. Fig. 4f and g show the cycling performance and
345 charge/discharge curves of the batteries with bare Zn anode and NFC/Al(OH)$_3$/PTFE@ Zn at the
346 current density of 2 A/g, respectively. The results reveal that the VO_2 || NFC/Al(OH)$_3$/PTFE
347 @Zn batteries deliver a high initial specific capacity of 406.2 mAh/g, and stabilizes at 381.6
348 mAh/g after 300 cycles, retenting 94% of the initial capacity. The utilization efficiency of the
349 prepared battery after 300 cycles was approximately 1% and N/P ratio was 130.02 . The cycling
350 continued untill 3300 cycles with the specific capacity of 292.2 mAh/g and 72% retention of
351 initial capacity, indicating an effectual long-term permanence with 100% coulombic efficiency.
352 The improved cycling life, higher specific capacity, and enhanced capacity retention could be

353 due to the improved wettability by the NFC/$Al(OH)_3$/PTFE coating layer, which regulated the
354 deposition of Zn^{2+} ions on the Zn anode surface, and inhibition of parasitic side reactions.
355 Moreover, the presence of PTFE layer on the Zn anode surface can reduce the electrode
356 corrosion. However, the initial specific capacity of VO_2 || bare Zn batteries was 398.4 mAh/g and
357 it dropped to 321 mAh/g after 300 cycles, with the capacity retention of 80.5%. For the batteries
358 with the bare Zn anode, the short circuit and failure happend after around 2000 hours with the
359 specific capacity of 265.6 mAh/g and 66.6% retention of initial specific capacity. This failure
360 probably results from the corrosion of the bare Zn anode, rapid growth of Zn dendrites, and the
361 associated side reactions such as hydrogen evolution.

362 The rate performance of VO_2 || bare Zn and VO_2 || NFC/$Al(OH)_3$/PTFE @Zn cells from 1
363 to 10 A/g is demonstrated in Fig. 5a. The results reveal that the specific capacity of VO_2 ||
364 NFC/$Al(OH)_3$/PTFE cell returned to the initial values after the cycling, showing appropriate
365 cycle stability and rate endurability. However, at 10 A/g the value of specific capacity of the
366 battery with coated Zn was slightly lower than that of the battery with bare Zn anode. The
367 slightly weaker performance of the VO_2 || NFC/$Al(OH)_3$/PTFE @Zn can be attributed to the
368 slower Zn^{2+} ion transfer through the NFC/$Al(OH)_3$/PTFE protective layer. As a result, when
369 designing the thickness and formulation of hybrid coating suspension, a balance between cycling
370 lifespan and rate performance needs to be considered. Fig. 5b illustrates the Galvanostatic
371 Charge-Discharge (GCD) behavior of the VO2 || NFC/Al(OH)3/PTFE @Zn cell across different
372 current densities. The enhanced performance exhibited by full batteries utilizing
373 NFC/Al(OH)3/PTFE @Zn anode are notably in line with the aforementioned observations, thus
374 reaffirming the efficacy of this strategies.

Fig. 5c illustrates the first three cycles of CV curves of VO_2 || NFC/$Al(OH)_3$/PTFE @Zn battery at a scan rate of 0.2 mV/s. The multi-step reversible insertion of Zn^{2+} ions into the VO_2 cathode led to the occurrence multiple anode and cathode peaks [34]. The overlapped CV curves indicate that coating the Zn anode with NFC/$Al(OH)_3$/PTFE led to a highly reversible reaction of the VO_2 cathode in the full cell battery. In order to evaluate the electrochemical reaction kinetics of the full cell battery with NFC/$Al(OH)_3$/PTFE @Zn, CV curves at 0.1, 0.2, and 0.5 mV/s were measured. As shown in Fig. 5d, two pairs of redox peaks can be observed, related to the redox reactions during charging/discharging process. The following equation was employed to investigate the relationship between peak currents (i) and scan rate (ϑ) [34]:

$$i = a\vartheta^b \tag{2}$$

where i represents the current, ϑ is the scan rate, and **a** and **b** are adjustable parameters. The b values of 0.5 and 1 show the reactions of diffusion control and capacitance control, respectively [35]. The log (i) versus log (ϑ) plot in Fig. 5e shows that the obtained b values corresponding to the peak 1 and peak 2 are 0.68 and 0.76, respectively, indicating that the electrochemical reactions responsible for these peaks are likely influenced by a combination of diffusion and capacitance effects. Moreover, as illustrated in Fig. 5e, the b values of peak 3 and peak 4 are equal to 0.98 and 0.99, respectively which indicates that the oxidation reactions are controlled by the capacitance reaction. It means that the rate of the reaction is determined by the charge transfer kinetics at the electrode-electrolyte interface. In other words, the electrochemical process occurs quickly because electrons can easily transfer between the electrode and the electroactive species in the electrolyte [36].

Cycling tests at 50°C with a current density of 2.5 mA/cm^2 (0.5 mAh/cm^2) was conducted to assess the performance of symmetric bare Zn and NFC/Al(OH)$_3$/PTFE@Zn batteries at higher temperature. The results have been included in Fig. S8. The findings indicate that the performance of bare Zn was unfavorable, with rapid short-circuit occurrences. However, the application of the protective layer significantly improved the cycling life of the battery. Despite the challenges posed by high temperatures, where increased kinetic energy and accelerated ion transportation may expedite dendrite formation, the coated layer demonstrated enhanced battery performance.

Table 1 presents a comparative analysis of the electrochemical performance of the batteries prepared in this study in relation to recently published papers that investigated zinc-ion batteries featuring various zinc protective layers. The findings in this table highlight that the utilization of an NFC/Al(OH)$_3$/PTFE protective layer on the zinc anode, as implemented in this study, demonstrated notable efficiency, particularly at elevated cycling numbers.

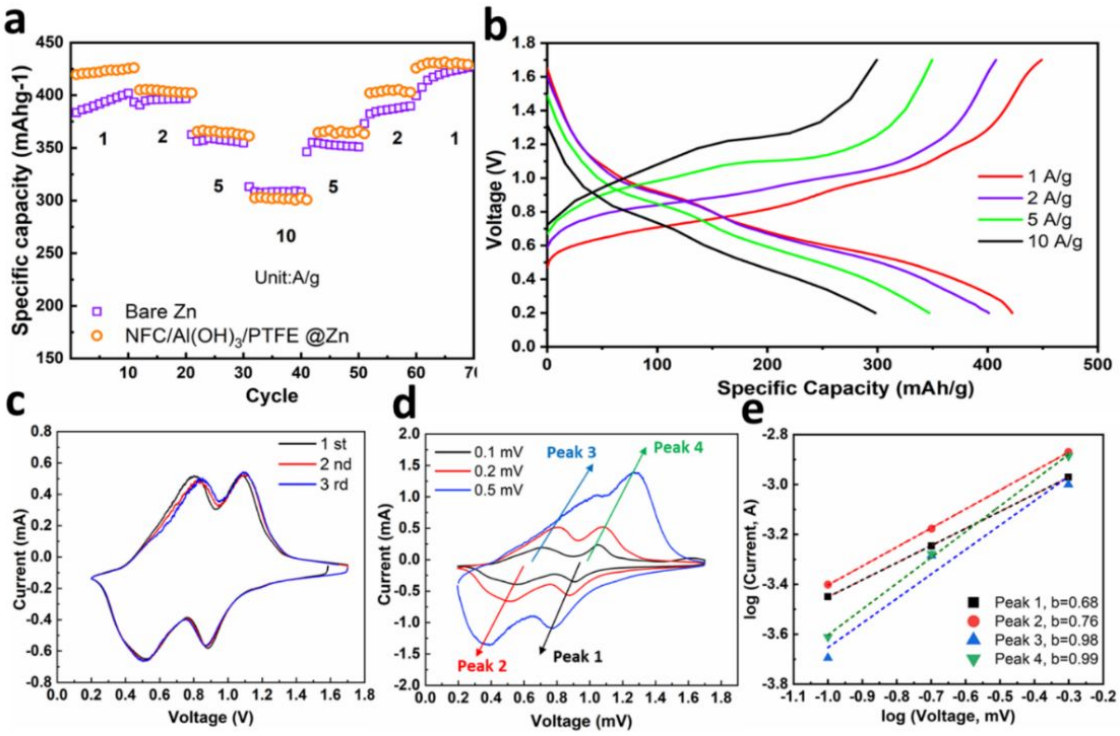

Fig. 5. Electrochemical performances of VO2||NFC/$Al(OH)_3$/PTFE @Zn batteries: (a) Rate performance at the current densities of 1, 2, 5, 10, 5, 2, and 1 A/g, (b) Charge/discharge profiles at various currents of the full cell with NFC/Al(OH)3/PTFE @Zn, (d) Cyclic voltammetry curve at 0.2 mV s^{-1} (c), cyclic voltammetry plots scanned at 0.1, 0.2, and 0.5 mV s^{-1}, and (e) log i versus log scan rate plots of VO2||NFC/$Al(OH)_3$/PTFE @Zn cells.

Table 1. Electrochemical properties of zinc-ion batteries featuring various protective layers, investigated in the present study and some of recent publications

Protective layer	Cathode	CD (A/g)	Specific Capacity (mAh/g)	Cycles	Efficiency (%)	Ref.
CNF/MXene	VO_2	2	357	500	93.3	19
PAN	MnVO	0.5	255	500	~60	37
PTFE/Porous Zn	MnV_2O_5	1	289.2	500	~37	30
LCNF/MXene	MnO_2	1	175.4	1000	50	10
NFC/$Al(OH)_3$/PTFE	VO_2	2	406.2	3300	72	This study

4. Conclusion

In this work, in-situ synthesis of $Al(OH)_3$ nanoparticle was carried out in the NFC network. PTFE was added to the NFC/ $Al(OH)_3$ suspension to produce a hybrid protective layer on the Zn anode surface, which regulates the zinc ion plating and stripping processes. The dense, hydrophilic, and porous structure of the coated layer modulated the diffusion and transport of Zn^{2+} ions on the zinc anode through active water restriction /zinc-sieving and reduced the corrosion and parasitic side reactions in the electrode/electrolyte interface. By taking advantage of the high reversibility, Zn//Zn symmetric cells maintained steady charge-discharge processes for more than 1000 hours at a current density of 1 $mAcm^{-2}$. The full battery with a VO_2 cathode showed excellent electrochemical performance, achieving high specific capacity (406.2 mAh/g at 2 A g^{-1}), acceptable rate performance, and long cycling stability for more than 3300 cycles. The proposed method and the detailed understanding of the mechanism presented in this study

represent a significant advancement in mitigating zinc dendrite formation, and can help inspire further research and development in the field of zinc-metal anodes and other aqueous metal-ion batteries.

Author information

Corresponding Authors

Corresponding emails: wuqing@lsu.edu and wxu26@lsu.edu

Author Contributions

The manuscript was written through contributions of all authors. All authors have given approval to the final version of the manuscript.

Conflicts of interest

There are no conflicts to declare.

Acknowledgments

The authors acknowledge the financial support USDA Forest Service/US Endowment (21-00157), Louisiana Board of Regents [LEQSF(2020-23)-RD-B-02] and National Science Foundation (2120640).

References

1 A. Dutta, S. Mitra, M. Basak and T. Banerjee, Energy Storage, 2023, 5, e339.

2 K. Mensah-Darkwa, C. Zequine, P. K. Kahol and R. K. Gupta, Sustainability, 2019, 11, 414.

3 R. K. Emmett and M. E. Roberts, J. Power Sources, 2021, 506, 230087.

4 W. Liu, M.-S. Song, B. Kong and Y. Cui, Adv. Mater., 2017, 29, 1603436.

5 D. Larcher and J.-M. Tarascon, Nat. Chem., 2015, 7, 19–29.

6 Y. Lv, Y. Xiao, L. Ma, C. Zhi and S. Chen, Adv. Mater., 2022, 34, 2106409.

7 S. Zhang, N. Yu, S. Zeng, S. Zhou, M. Chen, J. Di and Q. Li, J. Mater. Chem. A, 2018, 6, 12237–12243.

8 H. Jia, Z. Wang, B. Tawiah, Y. Wang, C.-Y. Chan, B. Fei and F. Pan, Nano Energy, 2020, 70, 104523.

9 Q. Yang, G. Liang, Y. Guo, Z. Liu, B. Yan, D. Wang, Z. Huang, X. Li, J. Fan and C. Zhi, Adv. Mater., 2019, 31, 1903778.

10 C. Liu, Z. Li, X. Zhang, W. Xu, W. Chen, K. Zhao, Y. Wang, S. Hong, Q. Wu, M. Li and C. Mei, Adv. Sci., 2022, 9, 2202380.

11 Z. Cai, Y. Ou, J. Wang, R. Xiao, L. Fu, Z. Yuan, R. Zhan and Y. Sun, Energy Storage Mater., 2020, 27, 205–211.

12 C. Ma, X. Wang, W. Lu, C. Wang, H. Yue, G. Sun, D. Zhang and F. Du, Chem. Eng. J., 2022, 429, 132576.

13 J. Yan, M. Ye, Y. Zhang, Y. Tang and C. C. Li, Chem. Eng. J., 2022, 432, 134227.

14 W. Han, H. Lee, Y. Liu, Y. Kim, H. Chu, G. Liu and W. Yang, Chem. Eng. J., 2023, 452, 139090.

15 Q. Song, J. Liang, S. Liu, Y. Zhang, J. Zhu and C. Zhu, Nano Res., 2022, 1–8.

16 W. Xu, K. Zhao, W. Huo, Y. Wang, G. Yao, X. Gu, H. Cheng, L. Mai, C. Hu and X. Wang, Nano Energy, 2019, 62, 275–281.

17 Z. Li, L. Ye, G. Zhou, W. Xu, K. Zhao, X. Zhang, S. Hong, T. Ma, M.-C. Li and C. Liu, Chem. Eng. J., 2023, 457, 141160.

18 Y. Liang, D. Ma, N. Zhao, Y. Wang, M. Yang, J. Ruan, G. Yang, H. Mi, C. He and P. Zhang, Adv. Funct. Mater., 2022, 32, 2112936.

19 W. Xu, X. Liao, W. Xu, K. Zhao, G. Yao and Q. Wu, Adv. Energy Mater., 2023, 2300283.

20 W. Zhou, M. Chen, Q. Tian, J. Chen, X. Xu and C.-P. Wong, Energy Storage Mater., 2022, 44, 57–65.

21 M. Shayan, J. Gwon, M. S. Koo, D. Lee, A. Adhikari and Q. Wu, Cellulose, 2022, 29, 9731–9751.

22 Q. Wu, C. Mei, J. Han, Y. Yue and X. Xu, J. For. Eng., 2018, 3, 1–9.

23 X. Wang, C. Yao, F. Wang and Z. Li, Small, 2017, 13, 1702240.

24 X. Yue, Q. Wang, K. Ao, J. Shi, X. Zhang, H. Zhao, K. Uyanga, Y. Yang and W. A. Daoud, J. Power Sources, 2023, 557, 232553.

25 J. Fu, H. Wang, P. Xiao, C. Zeng, Q. Sun and H. Li, Energy Storage Mater., 2022, 48, 191.

26 X. Du, Z. Zhang, W. Liu and Y. Deng, Nano Energy, 2017, 35, 299–320.

27 X. Zhang, J. Li, D. Liu, M. Liu, T. Zhou, K. Qi, L. Shi, Y. Zhu and Y. Qian, Energy Environ. Sci., 2021, 14, 3120–3129.

28 J. Si, R. Ma, Y. Wu, Y. Dong and K. Yao, J. Mater. Sci., 2022, 57, 8154–8166.

29 M. Goudarzi, D. Ghanbari, M. Salavati-Niasari and A. Ahmadi, J. Clust. Sci., 2016, 27, 25–38.

30 W. Guo, X. Bai, Z. Cong, C. Pan, L. Wang, L. Li, C. Chang, W. Hu and X. Pu, ACS Appl. Mater. Interfaces, 2022, 14, 41988–41996.

31 J. Cui, J. Liu, C. He, J. Li and X. Wu, J. Membr. Sci., 2017, 541, 661–667.

32 M. Liu, L. Yang, H. Liu, A. Amine, Q. Zhao, Y. Song, J. Yang, K. Wang and F. Pan, ACS Appl. Mater. Interfaces, 2019, 11, 32046–32051.

33 A. Pei, G. Zheng, F. Shi, Y. Li and Y. Cui, Nano Lett., 2017, 17, 1132–1139.

34 Y. Fang, X. Xie, B. Zhang, Y. Chai, B. Lu, M. Liu, J. Zhou and S. Liang, Adv. Funct. Mater., 2022, 32, 2109671.

35 Q. Pang, C. Sun, Y. Yu, K. Zhao, Z. Zhang, P. M. Voyles, G. Chen, Y. Wei and X. Wang, Adv. Energy Mater., 2018, 8, 1800144.

36 G. Fang, C. Zhu, M. Chen, J. Zhou, B. Tang, X. Cao, X. Zheng, A. Pan and S. Liang, Adv. Funct. Mater., 2019, 29, 1808375.

37 P. Chen, X. Yuan, Y. Xia, Y. Zhang, L. Fu, L. Liu, N. Yu, Q. Huang, B. Wang, X. Hu, Y. Wu and T. Van Ree, Adv. Sci., 2021, 8, 2100309.